Evaluation of a Coupled Modeling Approach for the Investigation of the Effects of SST Mesoscale Variability on the Atmosphere

Istvan Szunyogh[1], Eric Forinash[1], Gyorgyi Gyarmati[1],Yinglai Jia[2], Ping Chang[1,3], and R. Saravanan[3]

[1]Department of Atmospheric Sciences, Texas A&M University, College Station, Texas, USA.
[2]Physical Oceanography Laboratory Ocean University of China, Qingdao, China.
[3]Department of Oceanography, Texas A&M University, College Station, Texas, USA.

Key Points:

- A proper pair of estimates of the oceanic heat flux is crucial for the detection of the atmospheric response to SST mesoscale variability.
- Investigating the atmospheric effects of ocean mesoscale variability is more challenging than acknowledged in the literature.
- The atmospheric eddy kinetic energy equation can be used to analyze the synoptic scale response of the atmosphere to SST variability.

Corresponding author: I. Szunyogh, szunyogh@tamu.edu

Abstract

This study further evaluates the modeling approach of *Jia et al.* [2019] to investigate the potential effects of SST mesoscale variability on the atmospheric dynamics. The approach employs a global atmospheric circulation model coupled to a slab ocean model to produce two ensembles of simulations: one in which the ocean exhibits realistic SST mesoscale variability, and another in which the SST mesoscale variability is suppressed. The latter ensemble is produced by spatially filtering the SST analyses used for the estimation of the oceanic heat flux and the specification of the SST initial condition. The results of the present study, which focuses on the processes of the North Pacific, suggest that while the modeling approach yields the desired SST differences between the two ensembles at the mesoscales, it also introduces SST differences at the large scales that become the primary driver of the large scale differences in the simulated atmospheric flow. Diagnostics based on the eddy kinetic energy indicate that the large scale differences of the atmospheric flow lead to major differences in the dynamics of the jet stream and storm track. Because the large scale SST differences between the two ensembles are primarily driven by the differences between the prescribed estimates of the oceanic heat fluxes, finding a proper pair of those estimates is a necessary condition for the experiment design to detect the atmospheric response to SST mesoscale variability. The paper concludes with proposing a new strategy for the estimation of the oceanic heat fluxes.

Plain Language Summary

This study evaluates a modeling approach to investigate the potential effects of ocean sea surface temperature mesoscale (scales smaller than 100 km) variability on the atmospheric dynamics. The approach employs a global atmospheric circulation model coupled to a purely thermodynamical model of the ocean. Two ensembles of model simulations are prepared: one in which the ocean exhibits realistic sea surface temperature mesoscale variability, and another in which that variability is suppressed. The results of the present study, which focuses on the processes of the North Pacific, suggest that while the modeling approach yields the desired sea surface temperature mesoscale differences between the two ensembles, it also introduces differences at the larger scales, which become the primary driver of the differences in the simulated atmospheric flow. Because the larger scale sea surface temperature differences between the two ensembles are primarily driven by the differences between the estimates of the heat transport in the ocean, finding a proper pair of estimates is a necessary condition for the experiment design to detect the atmospheric response to sea surface temperature mesoscale variability. The paper concludes with proposing a new strategy for the estimation of the oceanic heat transfer.

1 Introduction

It is well established that the large-scale oceanic fronts associated with the Kuroshio Extension and the Gulf Stream anchor the entrance regions of the midlatitude atmospheric storm tracks of the Northern Hemisphere [e.g., *Nakamura et al.*, 2004, 2008]. It is also widely accepted that the SST anomalies associated with the ocean mesoscale eddies that form along the large scale oceanic fronts have a major effect on the atmospheric boundary layer [e.g., *Chelton and Xie*, 2010; *Small* et al., 2008; *Xie*, 2004]. The deeper tropospheric effects of SST mesoscale variability, however, are less understood and have been the subject of ongoing research. For instance, *Woollings* et al. [2010] found a subtle, but significant effect on the midlatitude storm tracks in simulations with a limited area version of the Hadley Centre's third generation atmospheric model. *Ma et al.* [2015, 2017] reported a poleward shift of the North Pacific storm track, with a deep tropospheric impact that extended to the west

coast of North America, in atmospheric simulations with the limited area Weather Research and Forecasting (WRF) model. *Foussard et al.* [2019] also found a polar shift of the storm track in idealized midlatitude channel model experiments with WRF, while *Zhang* et al. [2020] observed it in global atmospheric simulations with an earlier version of the Community Atmosphere Model (CAM4).

The aforementioned findings suggests that ocean mesoscale variability has a potentially significant deep tropospheric effect on the atmospheric circulation. The implications of the existence of such an effect would be important for both climate modeling and numerical weather forecasting. For instance, the ocean mesoscale eddies that form along the midlatitude oceanic fronts can persist for months [*Chelton et al.*, 2004] and may serve as a potential source of atmospheric predictability in the subseasonal-to-seasonal (S2S) time range [*Saravanan and Chang*, 2018]. (Identifying sources of S2S predictability has been an active area of research in recent years [e.g., *Lang et al.*, 2020; *Mariotti et al.*, 2020].)

The potential importance of the atmospheric effects of ocean mesoscale variability motivates the search for coupled atmosphere-ocean modeling approaches that could replace the current uncoupled, atmosphere-only modeling experiment designs to explore them. The two main challenges that a coupled approach must address are the extremely high computational cost of a fully coupled simulation at the required resolution and the large systematic errors (biases) that tend to develop in the ocean component of such a simulation. *Jia et al.* [2019] (JEA19 hereafter), with these challenges in mind, proposed the use of a high-resolution slab ocean model in the coupled simulations. This approach has a number of conceptually appealing features. First, the computational cost of the coupled simulations with a slab ocean model is significantly lower than that with a full ocean circulation model. Second, it can still simulate the nonlinear thermodynamical feedback between the atmosphere and ocean, eliminating the implicit assumption of the atmosphere-only modeling approaches that the heat capacity of the ocean is infinite, while it can also account for the oceanic heat transport by a prescribed oceanic heat flux field. Third, systematic SST errors (biases) are easier to control in a slab ocean than a full ocean circulation model [*Zuidema*, 2016]. Finally, in a potential operational forecast application, which requires the availability of real-time initial conditions for all prognostic model variables, it requires the availability of only an SST analysis for the ocean.

In their demonstration of the proposed approach, JEA19 carried out global simulation experiments with the Community Earth System Model (CESM) of the National Center for Atmospheric Research (NCAR), but they were able to present only a limited number of diagnostic results in a rapid communication paper. Our goal is to further analyze the simulation results of JEA19, with the hope that the investigation can lead to refinements of the modeling approach. While the simulations are global, we focus our attention on the dynamical processes of the North Pacific. The structure of the paper is as follows. Section 2 describes the design of the simulations of JEA19, with a special attention to the procedure for the estimation of the prescribed oceanic heat flux fields of the slab ocean model. The same section presents the atmospheric eddy kinetic energy equation of *Orlanski and Katzfey* [1991], which is our main diagnostic tool for the investigation of the dynamics of the storm track in the simulations of JEA19. Section 3 presents the diagnostic results, while section 4 draws the conclusions and proposes potential improvements to the design of the simulations.

2 Background

We first describe the prognostic equation of the slab ocean model, which governs the spatiotemporal evolution of the SST. We then explain the approach of JEA19 for the estimation of the oceanic heat flux, which is a prescribed input field of the

slab ocean model. We continue with an explanation of the approach of JEA19 to simulate the effect of ocean mesoscale variability on the atmospheric circulation by two ensembles of simulations: one in which the SST mesoscale variability is retained and another in which the SST mesoscale variability is suppressed. We refer to the former ensemble as the *control ensemble,* and the latter as the *filtered ensemble.* We conclude the section by introducing the atmospheric eddy kinetic energy equation.

2.1 The slab ocean model

A slab ocean model consists of a single mixed layer whose thermodynamical state depends on the horizontal Eulerian location $\mathbf{r}$ and time t. The thermal effects of the oceanic heat transport on the mixed layer is accounted for by the $Q_{ocn}(\mathbf{r},t)$ net outgoing heat flux at the bottom and side walls of the water column. The single prognostic equation of the model is

$$\frac{\partial T_{mix}}{\partial t}(\mathbf{r},t) = \frac{1}{\rho c_o h_{mix}(\mathbf{r})}\left[Q_{atm}(\mathbf{r},t) - Q_{ocn}(\mathbf{r},t)\right], \tag{1}$$

where $T_{mix}(\mathbf{r},t)$ is the SST (the temperature of the ocean mixed layer), ρ is the constant density of ocean water, c_o is the specific heat of ocean water, $h_{mix}(\mathbf{r})$ is the depth of the ocean mixed layer, $Q_{atm}(\mathbf{r},t)$ is the incoming heat flux from the atmosphere, and $Q_{ocn}(\mathbf{r},t)$ is the prescribed estimate of the net outgoing oceanic heat flux. For brevity, we will refer to $Q_{atm}(\mathbf{r},t)$ as the *atmospheric heat flux*, and to $Q_{ocn}(\mathbf{r},t)$ as the *oceanic heat flux*. (A negative value of $Q_{ocn}(\mathbf{r},t)$ indicates heating of the mixed layer, while a positive value indicates cooling.) In the experiments of JEA19, the parameters of Eq. (1) were $\rho = 1026$ kgm^{-3}, $c_0 = 3930$ Jkg^{-1}K^{-1}, and $h_{mix}(\mathbf{r})$ was prescribed from the *Levitus* [1982] Climatological Atlas of the World Ocean.

JEA19 obtained estimates of $Q_{ocn}(\mathbf{r},t)$ by first computing

$$Q_{atm}(\mathbf{r},t) = Q_{sol}(\mathbf{r},t) - Q_{long}(\mathbf{r},t) - Q_{sen}(\mathbf{r},t) - Q_{latent}(\mathbf{r},t) \tag{2}$$

from a 10-member ensemble of uncoupled atmospheric simulations with CESM that were forced by observations-based SST analyses. In Eq. (2), $Q_{sol}(\mathbf{r},t)$ is the net radiative heating of the ocean mixed layer by solar radiation, $Q_{long}(\mathbf{r},t)$ is the net long-wave radiative cooling of the ocean mixed layer, $Q_{sen}(\mathbf{r},t)$ is the net sensible heat flux from the ocean to the atmosphere, and $Q_{latent}(\mathbf{r},t)$ is the net latent heat flux from the ocean to the atmosphere. (It is important to notice that $Q_{atm}(\mathbf{r},t)$ is a nonlinear function of the SST, $T_{mix}(\mathbf{r},t)$). The initial conditions of the 10-member ensemble were independent of each other, but all members were forced by the same time series of SST and ice analyses: 0.25° spatial resolution, daily, 0000 UTC NOAA Optimum Interpolation Sea Surface Temperature and ICE (OISSTV2) analyses from December 2007. The particular time period was chosen, because it was the time of an unstable epoch of the Kuroshio Extension that produced active mesoscale ocean eddies and strong mesoscale SST anomalies, but was also a time when the El Niño-Southern Oscillation (ENSO) and the Pacific Decadal Oscillation (PDO) were nearly neutral. It was also the period investigated by *Ma et al.* [2015, 2017].

After computing $Q_{atm}(\mathbf{r},t)$ for each member of the ensemble of uncoupled atmospheric simulations, JEA19 computed $Q_{ocn}(\mathbf{r},t)$ for each member from Eq. (1), using finite-differences to approximate the SST tendencies from the SST analyses. Finally, they computed the average of $Q_{ocn}(\mathbf{r},t)$ over all ensemble members and times to obtain a time-independent estimate $Q_{slab}(\mathbf{r})$ of $Q_{ocn}(\mathbf{r},t)$. This static estimate was used as the prescribed input field $Q_{ocn}(\mathbf{r},t)$ of Eq. (1) at all times in the coupled simulations, that is, the actual prognostic equation of the slab ocean model was

$$\frac{\partial T_{mix}}{\partial t}(\mathbf{r},t) = \frac{1}{\rho c_o h_{mix}(\mathbf{r})}\left[Q_{atm}(\mathbf{r},t) - Q_{slab}(\mathbf{r})\right]. \tag{3}$$

While the temporal averaging removes the dependence of the estimate $Q_{slab}(\mathbf{r})$ on the transient changes in the atmospheric heat flux in the uncoupled simulations, it does not remove the dependence of $Q_{slab}(\mathbf{r})$ on the monthly mean atmospheric heat flux, $\overline{Q_{atm}}^{t}(\mathbf{r})$. This property of $Q_{slab}(\mathbf{r})$ follows from the equation

$$\overline{Q_{ocn}}^{t}(\mathbf{r}) = \overline{Q_{atm}}^{t}(\mathbf{r}) - \rho c_0 h_{mix}(\mathbf{r}) \overline{\delta T^a_{mix}}^{t}(\mathbf{r}), \tag{4}$$

which we obtain by taking the time mean of Eq. (1) and introducing the notations

$$\overline{Q_{ocn}}^{t}(\mathbf{r}) = \frac{1}{M}\int_{t_0}^{t_0+M} Q_{ocn}(\mathbf{r},t)dt, \tag{5}$$

$$\overline{Q_{atm}}^{t}(\mathbf{r}) = \frac{1}{M}\int_{t_0}^{t_0+M} Q_{atm}(\mathbf{r},t)dt, \tag{6}$$

$$\overline{\delta T^a_{mix}}^{t}(\mathbf{r}) = \frac{1}{M}\int_{t_0}^{t_0+M} \frac{\partial T_{mix}}{\partial t}(\mathbf{r},t)dt = \frac{1}{M}\left[T^a_{mix}(\mathbf{r},t_0+M) - T^a_{mix}(\mathbf{r},t_0)\right], \tag{7}$$

where t_0 is the time at the beginning of the uncoupled simulations, M is one month, and $T^a_{mix}(\mathbf{r},t_0+M)$ and $T^a_{mix}(\mathbf{r},t_0)$ are, respectively, the SST analyses at the end and the beginning of the simulations. Because $Q_{slab}(\mathbf{r})$ is the ensemble mean of $\overline{Q_{ocn}}^{t}(\mathbf{r})$ and ensemble averaging has no effect on the second term of the right-hand side of Eq. (4),

$$Q_{slab}(\mathbf{r}) = \overline{Q_{atm}}^{t,e}(\mathbf{r}) - \rho c_0 h_{mix}(\mathbf{r}) \overline{\delta T^a_{mix}}^{t}(\mathbf{r}), \tag{8}$$

where $\overline{Q_{atm}}^{t,e}(\mathbf{r})$ is the ensemble mean of $\overline{Q_{atm}}^{t}(\mathbf{r})$.

2.2 The control and filtered experiment

JEA19 carried out two 10-member ensembles of uncoupled atmospheric simulations to obtain two $Q_{slab}(\mathbf{r})$ estimates of the oceanic heating. In these simulations, the atmospheric and slab ocean model both had horizontal resolution $0.23^\circ \times 0.23^\circ$, while the atmospheric model had 30 vertical levels. The two ensembles differed in the treatment of the SST analysis fields that were used to compute the thermal forcing of the atmosphere by the ocean: one used $0.23^\circ \times 0.23^\circ$ resolution SST analyses, while the other used the same SST analyses after filtering the mesoscale variability by a $5^\circ \times 5^\circ$ boxcar averaging filter. The same sets of unfiltered and filtered SST analyses were used, in combination with the corresponding values of $\overline{Q_{atm}}^{t,e}(\mathbf{r})$, to approximate the left-hand side of Eq. (1) for the computation of $Q_{slab}(\mathbf{r})$. This procedure yielded the two estimates of $Q_{slab}(\mathbf{r})$: $Q^c_{slab}(\mathbf{r})$ for the unfiltered SST analyses, and $Q^f_{slab}(\mathbf{r})$ for the filtered SST analyses. (Hereafter, a superscribed c or f, respectively, indicates a scalar field of the control or filtered simulations.)

JEA19 carried out two ensembles of coupled simulations: one that used $Q^c_{slab}(\mathbf{r})$ and the unfiltered SST analyses from 0000 UTC, 1 December, 2007 as the SST initial condition, and another that used $Q^f_{slab}(\mathbf{r})$ and the filtered version of the same SST analysis as initial condition. The two experiments used the same 30-member ensemble of atmospheric initial conditions to produce two 30-member ensembles of month long simulations. (JEA19 showed that both ensembles developed a significant ensemble spread of the SST in response to the differences in the atmospheric conditions.) The ensemble based on the unfiltered SST analyses is the control ensemble, and the ensemble based on the filtered SST analyses is the filtered ensemble. We compute diagnostics for the two ensembles based on 6-hourly data from weeks 3 and 4 of the simulations. The motivation to discard the data from the first two weeks of the simulations is to reduce the effects of the initial transients on the diagnostics. To save computer resources, we compute all diagnostics based on the first 15 members of each ensemble. (We verified that 15 members were sufficient to reproduce the diagnostic results of JEA19 with good accuracy.)

2.3 The eddy kinetic energy equation

The eddy kinetic energy of *Orlanski and Katzfey* [1991] and *Orlanski et al.* [1995] is based on decomposing the atmospheric state variables into a time-mean and an eddy (transient) component. It was originally introduced to investigate the local energetics of individual weather events and has played an important role in developing the current understanding of storm track dynamics [e.g., *Chang and Orlanski*, 1993; *Chang*, 1993, 2005]. The equation is

$$\begin{aligned}\frac{\partial}{\partial t}\langle K_e\rangle \quad = \quad & \overbrace{-\langle\nabla\cdot\mathbf{v}K_e\rangle}^{1}\overbrace{-\langle\nabla\cdot\mathbf{v}'\phi'\rangle}^{2}\overbrace{-\langle\omega'\alpha'\rangle}^{3}\overbrace{-\langle\mathbf{v}'\cdot(\mathbf{v}'_{\mathbf{3}}\cdot\nabla_{\mathbf{3}})\,\overline{\mathbf{v}}-\mathbf{v}'\cdot\overline{(\mathbf{v}'_{\mathbf{3}}\cdot\nabla_{\mathbf{3}})\,\mathbf{v}'}\rangle}^{4} \\ & \overbrace{-\langle\nabla_p\cdot\omega'K_e\rangle}^{5}\overbrace{-\langle\nabla_p\cdot\omega'\phi'\rangle}^{6}\overbrace{+\langle(\text{Residue}\rangle)}^{7},\end{aligned} \tag{9}$$

where the Eulerian arguments $\mathbf{r}$ and t are not included in the notation for the sake of brevity. The equation is written using pressure p as the vertical coordinate. The angled bracket stands for the vertical mean

$$\langle A\rangle = \frac{1}{(p_t - p_b)}\int_{p_b}^{p_t} A(p)dp$$

of a scalar valued function A of the state for the layer between pressure levels p_b and p_t ($p_b > p_t$). In our diagnostic calculations, $p_b = p_s(\mathbf{r},t)$, where $p_s(\mathbf{r},t)$ is the surface pressure, and $p_t = 100\ hPa$. (The contribution of the different processes at the different vertical levels can be investigated be examining the vertical profiles of the integrand $A(p)$ for the different terms.) The prime indicates the eddy component of a variable, while the bar indicates its time-mean component. Because the time-mean is computed for a two-week period, we interpret it as the slowly varying component of the particular state variable. The state variables in the equation are the wind vector $\mathbf{v}_3 = (\mathbf{v},\omega)$ for pressure vertical coordinate, where u, v and $\omega = \partial p/\partial t$ are, respectively, the zonal, meridional and vertical component of the wind vector; $\mathbf{v} = (u,v)$ is the horizontal wind; $K_e = u'^2 + v'^2$ is the eddy kinetic energy density, ϕ is the geopotential, $\omega = dp/dt$ is the vertical velocity, and α is the specific volume. The spatial derivatives are represented by the del operators $\nabla_3 = (\nabla, \partial/\partial p)$ and $\nabla = (\partial/\partial x, \partial/\partial y)$, while the dot indicates the scalar product of two vectors.

Terms 1 (kinetic energy transport by the horizontal wind) and 2 (agesostrophic geopotential flux convergence) are transport terms that cannot be global sources or sinks of the eddy kinetic energy. Terms 5 and 6 are the vertical components of the transport described by terms 1 and 2 in the horizontal direction. While these terms are not zero, because of the possible transport of K_e and ϕ' through the p_t pressure surface, they are orders of magnitude smaller than the dominant terms and can be neglected. Term 3 is the baroclinc energy conversion term, which is almost always positive in the terrestrial atmosphere, indicating rising warm air or sinking cold air. It should always be verified, however, that a positive value of $-\omega'\alpha'$ (vertical temperature flux) is accompanied by a poleward (positive value in NH) of the meridional temperature flux, $v'T'$, to confirm that the vertical motions are associated with baroclinic instability rather than other forms of vertical motions. Term 4 is the sum of two terms, with the first term dominating. Because this dominant term describes the transfer of kinetic energy from the time mean flow to the eddies, it is called the barotropic energy conversion term. A negative value of this term indicates that kinetic energy is transferred from the eddies to the mean flow. Term 7 is the residue term, which can be calculated by computing the difference between the left-hand side of the equation and the sum of all other terms of the right-hand side of the equation. It represents the net effect of all processes not resolved by the other terms and the errors of the numerical approximations made to compute those terms. Because the most important processes

that the eddy kinetic energy equation does not resolve explicitly are dissipative, the residue term is typically negative.

We compute the terms of Eq. (9) every 6 h for each member of the two ensembles. For the computation of the time mean of the left-hand side of Eq. (9), which is necessary for the computation of the time-mean of the residue term, we take advantage of

$$\overline{\frac{\partial}{\partial t}\langle K_e\rangle}^{t} = \frac{1}{M'}\int_{t_0}^{t_0+L'}\frac{\partial}{\partial t}\langle K_e\rangle dt = \frac{1}{M'}[\langle K_e\rangle(t_0+M') - \langle K_e\rangle(t_0)], \tag{10}$$

where M' is two weeks. When we examine the vertical cross sections of the integrands in section 3.4, we also discuss the integrand $\nabla_p\cdot\omega' K_e$ of Term 5, because the transport of kinetic energy by the vertical motions induced by SST mesoscale variability may play a role in the vertical rearrangement of the eddy kinetic energy in the atmospheric column.

3 Results

We first show that the difference $\Delta Q_{slab}(\mathbf{r}) = Q^c_{slab}(\mathbf{r}) - Q^f_{slab}(\mathbf{r})$ between the two estimates of the oceanic heat flux drives, not only the mesoscale SST differences, but also the large scale SST difference between the two ensembles. This large scale SST difference is the primary driver of the large scale difference in the atmospheric flow, which also leads to major differences in the dynamics of the jet stream and storm track.

3.1 The estimates of the oceanic heat flux field

The top two panels of Fig. 1 show the $Q^c_{slab}(\mathbf{r})$ (top panel) and $Q^f_{slab}(\mathbf{r})$ (middle panel) estimates of the oceanic heat flux for the North Pacific. As can be expected, the boundaries between the regions of positive and negative values are sharper, and the absolute values of the local maxima and minima are larger in the control than the filtered experiment. The dominantly negative values of the two estimates indicate that oceanic heat transport is dominantly a heat source for the mixed layer for the winter-time oceanic conditions of the experiments. The exception is the narrow region of positive values off the coast of North America along the California Current, where oceanic heat transport is a net sink of heat for the mixed layer.

If $Q^c_{slab}(\mathbf{r})$ and $Q^f_{slab}(\mathbf{r})$ were both error-free estimates of the true oceanic heat flux, their difference $\Delta Q_{slab}(\mathbf{r})$ (bottom panel of Fig. 1) would only have mesoscale components. Because $\Delta Q_{slab}(\mathbf{r})$ has apparent large scale component, at least one, or more likely, both estimates include a large scale error component. To investigate the origin of this error component, we consider the equation

$$\Delta Q_{slab}(\mathbf{r}) = \Delta\overline{Q_{atm}}^{t,e}(\mathbf{r}) - \frac{\rho c_0 h_{mix}(\mathbf{r})}{M}\left[\Delta T^a_{mix}(\mathbf{r}, t_0+M) - \Delta T^a_{mix}(\mathbf{r}, t_0)\right], \tag{11}$$

where

$$\Delta T^a_{mix}(\mathbf{r}, t_0+M) = T^{ac}_{mix}(\mathbf{r}, t_0+M) - T^{af}_{mix}(tr, t_0+M), \tag{12}$$

$$\Delta T^a_{mix}(\mathbf{r}, t_0) = T^{ac}_{mix}(\mathbf{r}, t_0) - T^{af}_{mix}(\mathbf{r}, t_0), \tag{13}$$

This equation follows directly from Eq. (8). The second term of the right-hand side of Eq. (11) has only mesoscale components, because it represents the contribution of the changes in the analyzed SST mesoscale anomalies over the month. Thus the source of the large scale components of $\Delta Q_{slab}(\mathbf{r})$ must be the $\Delta\overline{Q_{atm}}^{t,e}(\mathbf{r})$ mean difference between the atmospheric heat fluxes computed from the two ensembles of uncoupled simulations. (We verified this conclusion by plotting $\Delta\overline{Q_{atm}}^{t,e}(\mathbf{r})$ and $\Delta T^a_{mix}(\mathbf{r}, t_0 +$

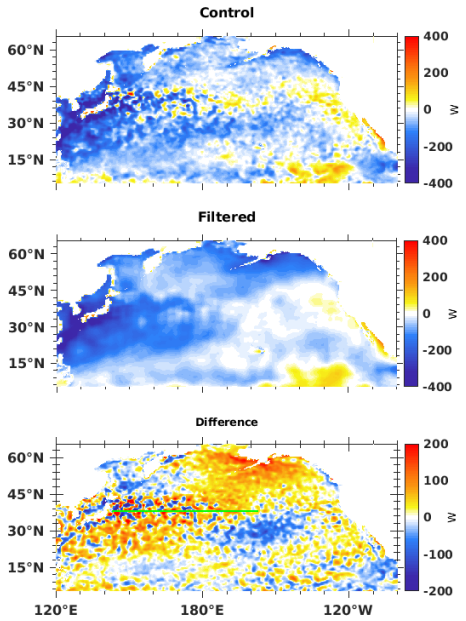

Figure 1. The $Q_{slab}(\mathbf{r})$ estimates of the oceanic heat flux used in the two ensembles. Shown are (color shades) (top) $Q^c_{slab}(\mathbf{r})$ and (middle) $Q^f_{slab}(\mathbf{r})$. A negative (positive) value indicates heating (cooling) of the ocean mixed layer. Also shown (bottom) is the differences $\Delta Q_{slab}(\mathbf{r})$ between the two estimates. The green line segment along 38°N indicates the position of the vertical cross-sections section 3.4. (Figs. 8–10).

$M) - \Delta T^a_{mix}(\mathbf{r}, t_0)$, but to save space, the two fields are not shown here.) $\overline{Q_{atm}}^{t,e}(\mathbf{r})$ (not shown) is negative in most of the North Pacific, with a large scale region of minima off the east coast of Japan. The nonzero large scale component of $\Delta\overline{Q_{atm}}^{t,e}(\mathbf{r})$ suggests that there is a large scale error in the mean atmospheric heat flux calculated from the ensemble of uncoupled simulations in at least one of those ensembles. It is more likely, however, that the mean atmospheric heat flux has large scale errors in both ensembles of uncoupled simulations. Hence, we interpret the large scale component of $\Delta Q_{slab}(\mathbf{r})$ as the difference of estimation errors introduced by the biases of the ensembles of uncoupled simulations. It is important to point out, however, that this difference would be zero, if the response of the atmospheric fluxes to the mesoscale SST forcing was linear in the uncoupled simulations.

What is the effect of the large scale components of $\Delta Q_{slab}(\mathbf{r})$ on the coupled simulations? We start the discussion of this problem with an examination of the mean differences,

$$b^c_{Tmix}(\mathbf{r}) = \overline{T^c_{mix}(\mathbf{r}, t) - T^{ac}_{mix}(\mathbf{r}, t)}^{t,e}, \quad (14)$$

$$b^f_{Tmix}(\mathbf{r}) = \overline{T^f_{mix}(\mathbf{r}, t) - T^{af}_{mix}(\mathbf{r}, t)}^{t,e}, \quad (15)$$

between the simulated and analyzed SST fields of the two ensembles of coupled simulations (Fig. 2). Here, $T^{ac}_{mix}(\mathbf{r}, t)$ and $T^{af}_{mix}(\mathbf{r}, t)$ are the unfiltered and filtered SST analyses, respectively. We emphasize that, in principle, $b^c_{Tmix}(\mathbf{r})$ and $b^f_{Tmix}(\mathbf{r})$ do not have be zero, because nonlinear effects in the evolution of the SST, which are introduced by the nonlinear feedback from the atmosphere, can lead to systematic differences between the simulated and analyzed SST. Thus the large scale patterns of

small magnitude systematic differences (less than 1.0°C at most locations) in the top two panels of Fig. 2 are not causes for concern at first sight. But, a comparison of the bottom panels of Fig. 1 and 2 suggests that the large scale patterns of the difference $b^c_{Tmix}(\mathbf{r}) - b^f_{Tmix}(\mathbf{r})$ closely resemble the large scale patterns of $\Delta Q_{slab}(\mathbf{r})$, except for the opposite signs. This relationship between the two fields suggests that the mean differences between the SST fields of the coupled simulations and the analyses are dominantly driven by $\Delta Q_{slab}(\mathbf{r})$, that is, by the differences between the biases of the atmospheric heat flux in the two ensembles of uncoupled simulations.

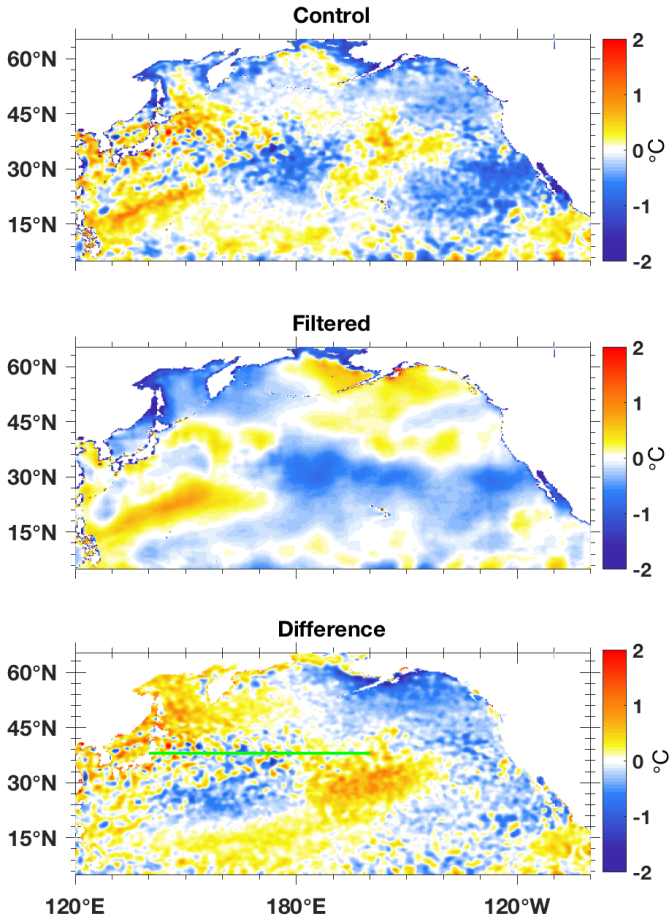

Figure 2. The mean of the differences between the SST and the SST analysis for the two ensembles. Shown are (color shades) the systematic SST differences for (top) the control ensemble, $b^c_{mix}(\mathbf{r})$ and (middle) filtered ensemble, $b^f_{mix}(\mathbf{r})$. A negative value indicate that the mean SST is lower (higher) in the simulations than the analyses. Also shown (bottom) is the difference $b^c_{mix}(\mathbf{r}) - b^f_{mix}(\mathbf{r})$ between the fields of the top two panels. The green line segment along 38°N indicates the position of the vertical cross-sections described in section 3.4. (Figs. 8–10).

3.2 Mean SST, and the Mean Atmospheric Flow

The mean SST fields of the two ensembles (Fig. 3, top two panels) and their difference (Fig. 3, bottom panel) show that JEA19 achieved their goal to maintain the SST mesoscale variability in the control ensemble and suppress it in the filtered ensemble. Most importantly, the SST mesoscale anomalies associated with the mesoscale eddies of the Kuroshio Extension (west of the dateline along the green line segment in the figure) are clearly present in the SST difference field $\Delta\overline{T}^{t,e}_{mix}(\mathbf{r})$. Elsewhere, however, the large scale differences dominate, which is not surprising in light of the results shown in Fig. 2, considering that

$$\Delta\overline{T}^{t,e}_{mix}(\mathbf{r}) = \Big[b^c_{mix}(\mathbf{r}) - b^f_{mix}(\mathbf{r})\Big] + \overline{T^{ac}_{mix}(\mathbf{r},t) - T^{af}_{mix}(\mathbf{r},t)}^{t,e}. \tag{16}$$

Based on this equation, the field in the bottom panel of Fig. 3 (left-hand side term) should look like the field in the bottom panel of Fig. 2 (first term of the right-hand side), except for the footprints of the persistent mesoscale anomalies (second term of the right-hand side). The most important such anomalies in the North Pacific are the mesoscale eddies of the Kuroshio Extension. Because the large scale component of $\Delta Q_{slab}(\mathbf{r})$ drives the large scale component of $\Big[b^c_{mix}(\mathbf{r}) - b^f_{mix}(\mathbf{r})\Big]$, it also drives the large scale component of $\Delta\overline{T}^{t,e}_{mix}(\mathbf{r})$. From an atmospheric point of view, the close relationship between the large-scale components of $\Delta Q_{slab}(\mathbf{r})$ and $\Delta\overline{T}^{t,e}_{mix}(\mathbf{r})$ is important, because by that relationship, $\Delta Q_{slab}(\mathbf{r})$ also controls the large scale differences of the mean atmospheric flow in the lower troposphere: at location where $\Delta\overline{T}^{t,e}_{mix}(\mathbf{r})$ is higher, the mean geopotential height difference $\Delta\overline{z}^{t,e}(\mathbf{r})$ is also higher near the surface (Fig. 4, bottom panel). The strong influence of $\Delta Q_{slab}(\mathbf{r})$ on the mean geopotential height field is not limited to the lower troposphere (Fig. 3). In fact, the small ($|\Delta\overline{z}^{t,e}|(\mathbf{r}) \leq$4 gpm) differences near the surface (bottom panel) translate to differences up to about 20 gpm in the middle troposphere (middle panel), and 60 gpm in the upper troposphere (top panel). This vertical profile of the geopotential height differences reflects an about 50-55 gpm difference of the atmospheric scale height, which would corresponds to a 1.7 K difference of the air temperature in an isothermal atmosphere. While the dominant large scale features of the $\Delta\overline{z}^{t,e}(\mathbf{r})$ field shift further and further to the east with height (compare the contour lines in the three panels of Fig. 4), they are clearly anchored by the dominant large scale features of $\Delta\overline{T}^{t,e}_{mixed}(\mathbf{r})$, that is, the large scale features of $\Delta Q_{slab}(\mathbf{r})$. In sections 3.3 and 3.4, we will show that the large scale features of $\Delta\overline{z}^{t,e}(\mathbf{r})$ have a major influence on the differences between the synoptic scale energy conversion processes in the two ensembles.

3.3 Vertically integrated diagnostics of the energy conversion

3.3.1 Eddy kinetic energy

The North Pacific storm track is the region of high eddy kinetic energy (warm color shades) in the top two panels of Fig. 5. The eddy kinetic energy is lower in the control experiment along and directly downstream of the Kuroshio Extension region (bottom panel). Further downstream, in the region of the relative ridge (in the mean geopotential height difference field) over the west coast, the eddy kinetic energy becomes higher in the control experiment. This spatial distribution of the eddy kinetic energy suggests that in the control experiment the upstream generation of eddy kinetic energy is reduced and its downstream propagation is modified by the changes in the large-scale atmospheric flow.

3.3.2 Baroclinic energy conversion

For the examination of the causes of the reduction of the upstream eddy kinetic energy production, we first recall that the main source of eddy kinetic energy of the

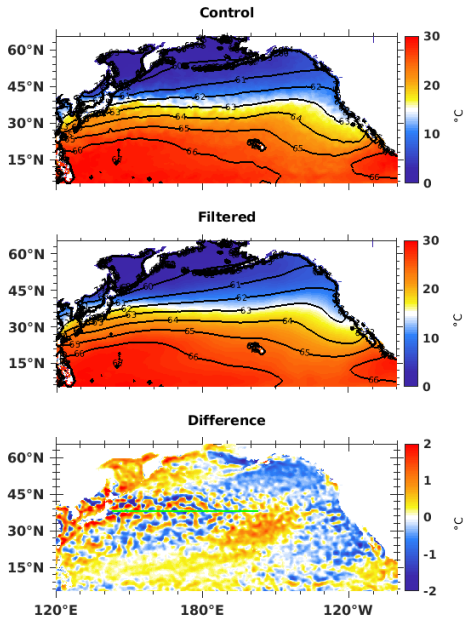

Figure 3. The mean SST field for the two ensembles. Shown are (color shades) $\overline{T}^{t,e}_{mixed}(\mathbf{r})$ and (contours with interval 1 gpm) $\overline{z}^{t,e}(\mathbf{r})$ at 992 hPa for the (top) control experiment and (middle) filtered experiment. Also shown (bottom) is the differences $\Delta\overline{T}^{t,e}_{mixed}(\mathbf{r})$ between the SST fields of the top two panels. The green line segment along 38°N indicates the position of the vertical cross-sections described in section 3.4 (Figs. 8–10).

extratropical storm tracks is baroclinic energy conversion. The differences in the baroclinic eddy kinetic energy production (Fig. 6) suggest that the intensity of the process is reduced in its main region, the region of the Kuroshio Extension, except for a small region northeast of Japan.

The primary role of the synoptic scale transient atmospheric motions induced by baroclinic instability is to reduce the zonal thermal imbalance (meridional temperature gradient) in the large scale atmospheric flow by the poleward transport of heat. The pair of large scale regions of relative cooling and heating in the ocean mixed layer along the Kuroshio Extension (Fig. 1) leads to a weaker meridional temperature gradient in the atmosphere. Hence, the synoptic scale atmospheric eddies are required to transport less heat in the control ensemble, which is consistent with the lower intensity of the baroclinic energy conversion. It should be kept in mind, however, that the pair of large scale regions of relative oceanic cooling and heating were introduced by the differences between the atmospheric heat fluxes computed from the uncoupled simulations.

3.3.3 Barotropic energy conversion

While an important global sink, barotropic energy conversion can be a source of eddy kinetic energy in a large geographical region. In the simulations of JEA19, such a region is the narrow, zonally elongated region around the core of the jet stream off the coast of Japan (Fig. 7, top two panels). In this region, which extends further to the east in the control experiment, kinetic energy is transferred from the jet stream to the eddies. Because of the more intense transfer of kinetic energy to the waves from the slowly varying component of the atmospheric flow in the upstream region of

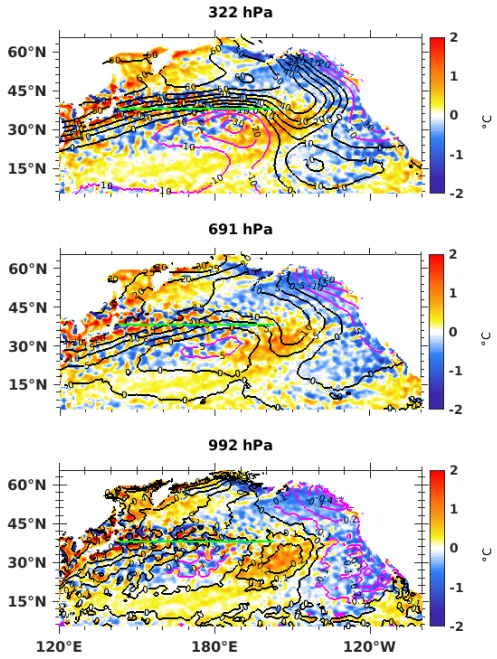

Figure 4. Illustration of the relationship between the mean SST differences and the differences in the atmospheric mean flow in the two ensembles. Shown are (color shades) $\overline{T}^{t,e}_{mixed}(\mathbf{r})$ and (contours) the $\overline{z}^{t,e}(\mathbf{r})$ difference field at (bottom) 992 hPa, (middle) 691 hPa, and (top) 322 hPa. Black contours indicate positive, while magenta contours negative values. The contour intervals are 0.1 gpm, 5 gpm, and 10 gpm at 992 hPa, 691 hPa, and 322 hPa, respectively. The green line segment along 38°N indicates the position of the vertical cross-sections described in section 3.4 (Figs. 8–10).

the storm track, and the less intense transfer of the kinetic energy from the waves in the downstream region, barotropic energy conversion is a relative source of the eddy kinetic energy in the control experiment. Since the magnitude and direction of the barotropic energy transfer strongly depends on the slowly varying component of the atmospheric flow, the differences of the large scale atmospheric flow between the two ensembles, which are forced by the large scale component of ΔQ_{slab}, have a major effect on the barotropic energy conversion in the simulations.

3.3.4 Transport processes and residue

The eddy kinetic energy field produced by baroclinic and barotropic energy conversion is rearranged by the two transport processes (Terms 1 and 2, results not shown). The net eddy kinetic energy transport by the horizontal flow (Term 1) is negative in the main region of baroclinic eddy kinetic energy production along the Kuroshio Extension. Because this region is smaller in the control experiment, there is a region around 160°W, 42°N, in which the net transport is positive in the control experiment, but negative in the filtered experiment. In addition, the difference is negative in the northeast corner of the Pacific, where the net transport is negative in the control and positive in the filtered experiment. As expected, the magnitude of the term (Term 2) that describes the other horizontal transport process, the agesostrophic geopotential flux convergence, is smaller than the magnitude of the terms that described the other

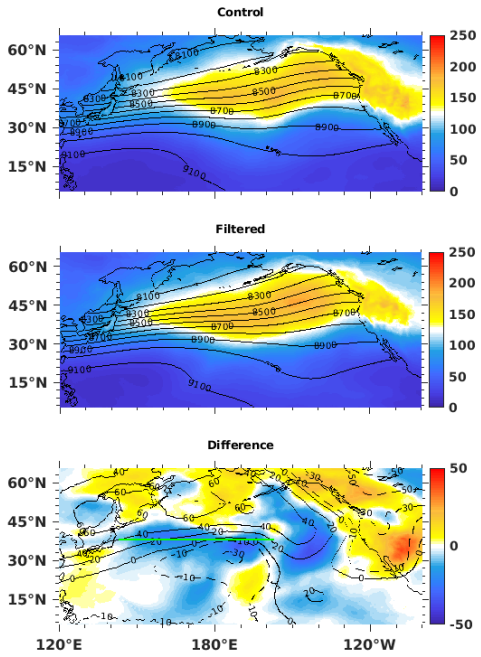

Figure 5. The vertically averaged mean eddy kinetic energy in the two ensembles. Shown are (color shades) $\overline{\langle K_e \rangle}^{t,e}$ and (contours) $\overline{z}^{t,e}(\mathbf{r})$ at 322 hPa for (top) the control experiment and (middle) the filtered experiment. Also shown are (bottom) the differences between the fields of the top two panels. The green line segment along 38°N indicates the position of the vertical cross-sections described in section 3.4 (Figs. 8–10).

processes in both experiments. The magnitude of the differences, however, is comparable to that of the other processes. Most importantly, the agesostrophic geopotential flux convergence is a relative source of the eddy kinetic energy in the region of the relative trough over western North America in the control experiment. Finally, for completeness, the residual term is dominantly negative in both experiments as expected, but it acts as a relative source over western North America in the control experiment.

3.4 Vertical profiles of the diagnostics of energy conversion

We further investigate the differences between the energy conversion processes in the region of the Kuroshio Extension, along the latitude segment marked by a green line in Figs. 1–6, with the help of vertical cross-sections of the processes. The mesoscale SST anomalies associated with the eddies of the Kuroshio Extension have significant amplitudes west of the dateline.

We recall that we found that the the vertically integrated eddy kinetic energy production by baroclinic instability was less intense in the control experiment. The vertical cross section of the baroclinic energy conversion (Fig. 8) suggests that the reduction in the vertically integrated term is the result of a mixture of enhancements and reductions at the different pressure levels. Reductions dominate in the mid-troposphere east of 150°N, where the mean zonal wind speed is also reduced. Because the reduction of the zonal wind speed becomes more significant with height, the zonal wind

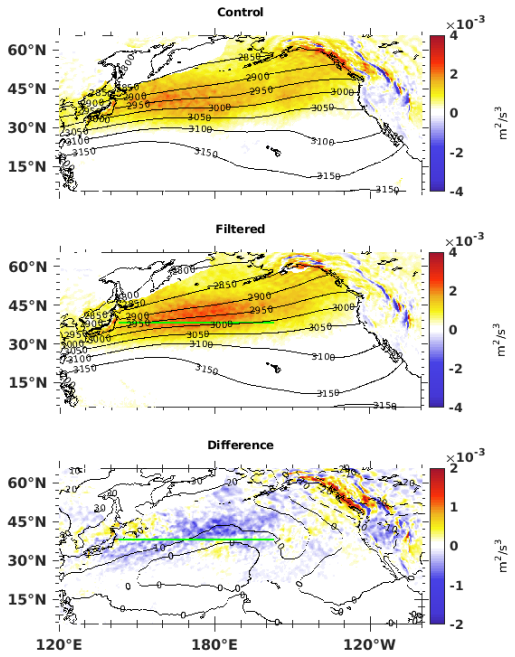

Figure 6. The vertically averaged mean baroclinic energy conversion in the two ensembles. Shown are (color shades) $-\overline{\langle\omega'\alpha'\rangle}^{t,e}$ for the locations where $v'T' > 0$ and (contours) $\overline{z}^{t,e}(\mathbf{r})$ at 691 hPa for (top) the control experiment and (middle) the filtered experiment. Also shown are (bottom) the differences between the fields of the top two panels. The green line segment along 38°N indicates the position of the vertical cross-sections described in section 3.4 (Figs. 8–10).

shear is also reduced except for the lowest atmospheric layer (below about 800 hPa) east of 175°E. As the strength of baroclinic instability is proportional to the vertical wind shear, the weakened wind shear plays an important role in the reduced intensity of the baroclinic energy conversion. In addition to the wind shear, the strength of the baroclinic instability also depends on the static stability of the atmosphere: a stronger static stability leads to a weaker baroclinic instability. The static stability (not shown) is generally higher in the control experiment below the 700 hPa level, which contributes to the weakened baroclinic instability in that layer. While the static stability is reduced in the layer between 700 hPa and 300 hPa, the Eady index of baroclinic instability (Fig. 9) indicates that the reduced wind shear more than compensates for that effect. Here, we define the Eady index by the mean daily growth rate of the most unstable mode of the Eady model of baroclinic instability. This growth rate is $e^{\sigma T}$, where

$$\sigma(\lambda, z) = 0.31 \frac{f}{\overline{N}} \frac{\partial \overline{u}}{\partial z}(\lambda, z), \tag{17}$$

T =24 h, $f = 10^{-4}$ is the the Coriolis parameter, and $\overline{N}(\lambda, z)$ is the Brunt-Vaisala frequency (the measure of static stability) for the mean flow. Baroclinic instability is enhanced only west of 170°E and only near the surface, where one expects to see the strongest mesoscale ocean eddy influence on the atmosphere. East of 170°E near the surface, and everywhere in the layer between 800 hPa and 400 hPa, baroclinic instability is greatly reduced, which is likely to be effect of the change in the large scale SST.

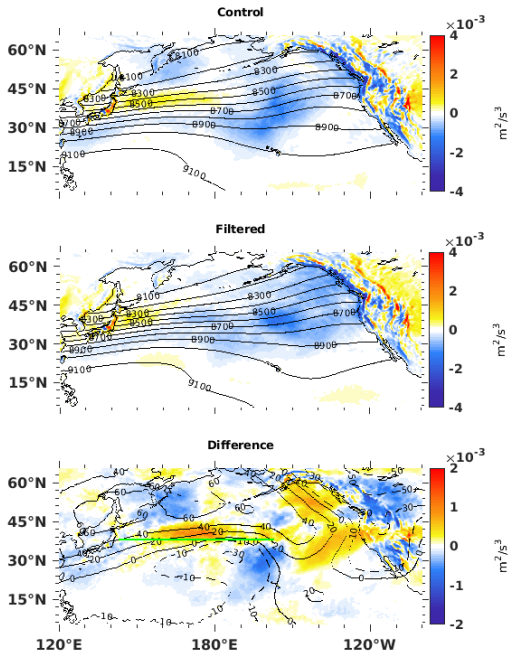

Figure 7. The vertically averaged mean barotropic eddy kinetic energy conversion in the two ensembles. Shown are (color shades) $-\overline{\langle \mathbf{v}' \cdot (\mathbf{v}'_{\mathbf{3}} \cdot \nabla_{\mathbf{3}}) \overline{\mathbf{v}}^{t,e}}$ and (contours) $\overline{z}^{t,e}(\mathbf{r})$ at 691 hPa for (top) the control experiment and (middle) the filtered experiment. Also shown are (bottom) the differences between the fields of the top two panels. The green line segment along 38°N indicates the position of the vertical cross-sections described in section 3.4 (Figs. 8–10).

Finally, we note that we also investigated the vertical profile of the vertical eddy kinetic energy transport (result not shown). The results showed that the vertical motions excited by the ocean eddies lead to a more efficient vertical transport of the eddy kinetic energy only in the layer between 850 hPa and 700 hPa.

4 Summary and Conclusions

We investigated dynamical processes in the model simulations of JEA19 that were carried out with a configuration of the NCAR CESM, in which the atmosphere was thermally coupled to a slab ocean. JEA19 generated two ensembles of simulations: while the quarter-degree horizontal resolution of both ensembles was sufficient to permit mesoscale SST variability, that variability was suppressed in one of the ensembles. Our study focused on the processes of the North Pacific region, for which we showed that the large scale differences of the atmospheric flow between the two ensembles were dominantly driven by the systematic large scale SST differences between the two ensembles. We demonstrated that these large scale SST differences were forced by the large scale differences between the estimates of the oceanic heat flux that were used in the two ensembles. We argued that the differences between the two estimates were the result of differences of the atmospheric heating field between the two ensembles of uncoupled simulations that produced those estimates. Diagnostics based on the atmospheric eddy kinetic energy equation revealed that the differences in the large scale atmospheric flow led to major differences in the dynamics of the North Pacific Jet Stream and Storm Track. Combining the aforementioned results, we conclude

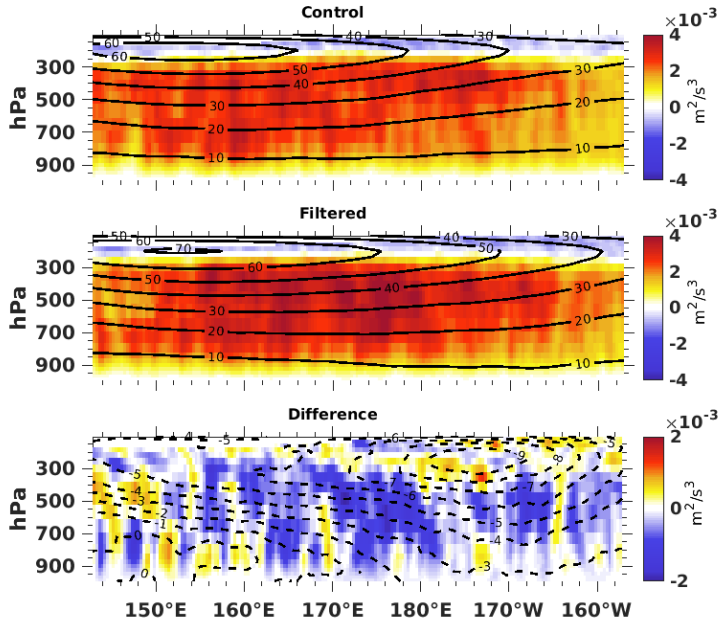

Figure 8. Vertical cross-section of the baroclinic energy conversion along the Kuroshio Extension in the two ensembles. Shown are the vertical cross sections of (color shades) $\overline{\omega'\alpha'}^{t,e}$ and (contours) $\overline{u}^{t,e}(\mathbf{r})$, where $u(\mathbf{r},t)$ is the zonal wind speed, for (top) the control experiment and (middle) the filtered experiment. Also shown are (bottom) the differences between the fields of the top two panels.

that the differences of the atmospheric response between the two ensembles of coupled simulations were primarily driven by the atmospheric response to the mesoscale variability of the SST forcing in the uncoupled simulations that provided the estimates of the oceanic heat flux.

Our results suggest that the investigation of the atmospheric effects of ocean mesoscale variability is a more challenging modeling problem than as it has been acknowledged in the literature. In particular, studies based on atmosphere-only uncoupled simulations make the implicit assumption that the heat capacity of the ocean is infinite. Such an assumption can made only because an uncoupled simulation is free to violate the heat equation for the ocean mixed layer, Eq. (1). More specifically, based on our earlier arguments, any uncoupled model experiment that produces a large scale difference of the atmospheric heat flux violates this equation. Hence, the atmospheric response detected in an uncoupled experiment critically depends on the biases of the atmospheric heat flux in the simulations. What makes controlling these biases particularly challenging is that the response of the atmospheric heat flux to mesoscale SST variability is apparently nonlinear. This suggests that taking the feedback from the atmosphere to the SST also into account, which can only be done in a coupled framework, may be essential for the detection of the atmospheric response to SST mesoscale variability. While there has been a recent study [*Small* et al., 2019] to investigate the lower tropospheric effect of ocean mesoscale variability on the mid-latitude storm tracks in a fully coupled framework, the natural first-step extension of the more common uncoupled approach is to employ a slab ocean model in a coupled system. Using a slab ocean model greatly reduces the computational cost and makes

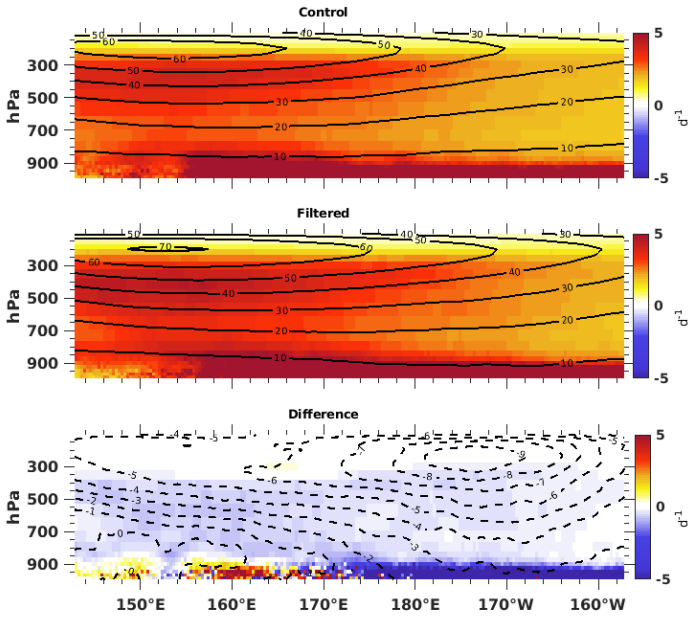

Figure 9. Vertical cross-section of the strength of the baroclinic instability along the Kuroshio Extension in the two ensembles. Shown are the vertical cross sections of (color shades) $\overline{e^{\sigma T}}^{t,e}$ and (contours) $\overline{u}^{t,e}(\mathbf{r})$ for (top) the control experiment and (middle) the filtered experiment. Also shown are (bottom) the differences between the fields of the top two panels.

handling the SST biases much more manageable compared with using a full ocean circulation model.

A strategy based on using a slab ocean model must ensure that spurious effects on the large scale SST by the estimates of the ocean heat flux do not dominate over the effects of the nonlinear feedback from the atmosphere. To be precise, there should be no large scale differences between the two estimates of the oceanic heat flux. A straightforward approach to achieve this goal would be to first compute an estimate of the oceanic heat flux field for the control ensemble and then obtain the estimate for the filtered ensemble by filtering the control estimate. It should be pointed out, however, that if the estimate for the control ensemble would be still computed from an ensemble of uncoupled simulations, both estimates would include a component related to the bias of the atmospheric heating in the uncoupled simulations. While this component would cancel out in the difference $\Delta Q_{slab}(\mathbf{r})$, it would still have an effect on the large scale SST biases of the uncoupled simulations.

One potentially effective approach to minimize the effect of biases of the uncoupled simulations on the coupled simulations would be to use an iterative algorithm for the estimation of the oceanic heating for the control ensemble, $Q^c_{slab}(\mathbf{r})$. In iteration k, the mean difference $b^{(k)}(\mathbf{r})$ between the simulated and analyzed SST would be computed as

$$b^{(k)}(\mathbf{r}) = \overline{T^{(k)}_{mix}(\mathbf{r},t) - T^{a}_{mix}(\mathbf{r},t)}^{t,e}, \tag{18}$$

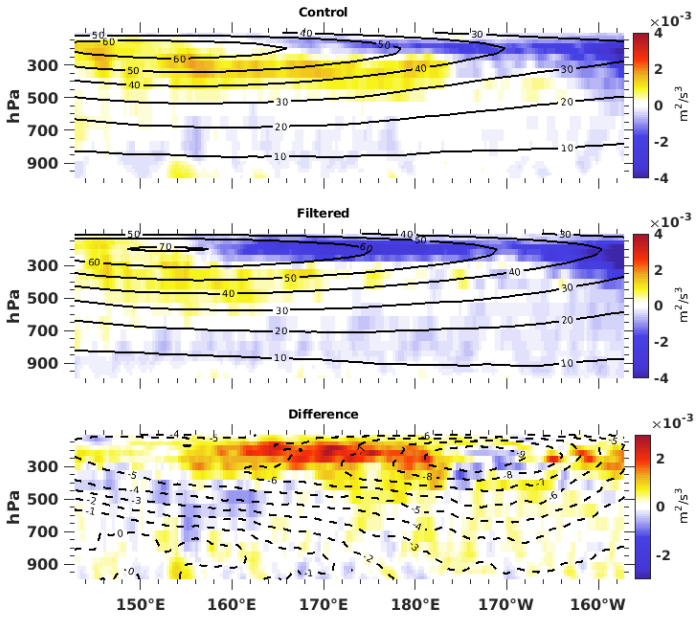

Figure 10. Vertical cross-section of the barotropic energy conversion along the Kuroshio Extension in the two ensembles. Shown are the vertical cross sections of (color shades) $\overline{\mathbf{v}' \cdot (\mathbf{v}'_\mathbf{3} \cdot \nabla_\mathbf{3})\,\overline{\mathbf{v}}}^{t,e}$ and (contours) $\overline{u}^{t,e}(\mathbf{r})$ for (top) the control experiment and (middle) the filtered experiment. Also shown are (bottom) the differences between the fields of the top two panels.

where $T^{(k)}_{mix}(\mathbf{r},t)$ is the mean SST for the coupled simulations of iteration k. The formula

$$\begin{aligned} Q^{(k)}_{slab}(\mathbf{r}) &= Q^{(k-1)}_{slab}(\mathbf{r}) + \delta Q^{(k)}_{slab}(\mathbf{r}), \\ \delta Q^{(k)}_{slab}(\mathbf{r}) &= -\frac{2b_{Tmix}(\mathbf{r})}{M\rho c_o h_{mix}(\mathbf{r})}, \end{aligned} \tag{19}$$

would then yield an updated estimate $Q^{(k)}_{slab}(\mathbf{r})$ of the oceanic heating. The initial estimate $Q^{(0)}_{slab}$ for $k = 1$ could be computed as in JEA19, based on an ensemble of uncoupled simulations. This algorithm would eliminate the systematic differences between the simulated and analyzed SST after one iteration, if the response of $b^{(k)}(\mathbf{r})$ to the correction $\delta Q^{(k)}_{slab}(\mathbf{r})$ was linear. Even if the response would be nonlinear, which is likely to be the case, the hope is that the magnitude $|b^{(k)}(\mathbf{r})|$ of $b^{(k)}(\mathbf{r})$ would satisfy $|b^{(k)}(\mathbf{r})| < |b^{(k-1)}(\mathbf{r})|$ for at least the first few iterations. The process would be stopped and $Q^{(k)}_{slab}(\mathbf{r})$ would become the estimate Q^{c}_{slab} once a desired small value of $|b^{(k)}(\mathbf{r})|$ was reached or the value of $|b^{(k)}(\mathbf{r})|$ could not be reduced further.

Finally, we note that future experiments investigating the atmospheric effects of SST mesoscale variability should strongly consider suppressing the SST mesoscale variability only in limited geographical regions rather than globally. Such an approach would allow for the separation of the effects of the different type ocean mesoscale anomalies (e.g., mesoscale eddies of the midlatitude oceanic fronts vs. tropical anomalies) and could also help to reduce the magnitude of the large scale SST differences.

Acknowledgments

This research has been conducted as part of the NOAA MAPP S2S Prediction Task Force and supported by NOAA grant NA16OAR4311082. Yinglai Jia was supported by National Key R&D Program of China (2017YFC1404101), and the Strategic Priority Research Program of the Chinese Academy of Sciences (Grant No. XDA11010203). Using an iterative algorithm for the estimation of the oceanic heat fluxes was first suggested by one of the anonymous reviewers of JEA19. The model simulation data of JEA that were used for this study are publicly available at https://doi.pangaea.de/10.1594/PANGAEA.897395.

References

Ahmadi-Givi, F., Craig, G. C., and Plant., S., (2004). The dynamics of a midlatitude cyclone with a very strong latent-heat release. *Q. J. R. Meteorol. Soc.* 130, 295–323.

Barsugli, J. J., and Battisti, D. S., (1998). The basic effects of atmosphere-ocean thermal coupling on midlatitude variability. *J. Atmos. Sci.* 55, 477–493.

Chang, E. K. M., (1993). Downstream development of baroclinic waves as inferred from regression analysis. *J. Atmos. Sci.* 50, 2038–2053.

Chang, E. K. M., (2005). The impact of wave packets propagating across Asia on Pacific cyclone development. *Mon. Wea. Rev.* 133, 1998–2015.

Chang, E. K. M., and I. Orlanski (1993). On the dynamics of a storm track. *J. Atmos. Sci.* 50, 999–1015.

Charney, J. G., (1947). The dynamics of long waves in a baroclinic westerly current. *J. Meteorol.* 6, 371–385.

Chelton, D. B., and Xi., S. P., (2010). Coupled ocean-atmosphere interactions at oceanic mesoscales. *Oceanography* 23, 52–69.

Chelton, D. B., Schlax, M. G., Freilich, M. H., and Milliff, R. F., (2004). Satellite measurements reveal persistent small-scale features in ocean winds. *Science* 303, 978–983.

Dee, D. P., Uppala, S. M., Simmons, A. J., Berrisford, P., Poli, P., Kobayashi, S., Vitart, F. (2011). The ERA-Interim reanalysis: Configuration and performance of the data assimilation system. *Q. J. R. Meteorol. Soc.* 137, 553–597.

Eady, E. T., (1949). Long waves and cyclone waves. *Tellus* 1, 33–52.

Feldstein, S. B., (2000). The timescale, power spectra, and climate noise properties of teleconnection pattern. *J. Climate* 13, 4430–4440.

Foussard, A., Lapeyre, G., and Plougonven, R. (2019). Storm track response to oceanic eddies in idealized atmospheric simulations. *J. Climate* 32, 444–463.

Jia, Y., Chang, P., Szunyogh, I., Saravanan, R., and Bacmeister, J. T. (2019). A modeling strategy for the investigation of the effect of mesoscale SST variability on atmospheric dynamics. *Geophys. Res. Lett.* 46, 3982–3989.

Lang, A., Pegion, K., and Barnes, E. A. (2020). Introduction to special collection: "Bridging Weather and Climate: Subseasonal-to-seasonal (S2S) prediction". *Journal of Geophysical Research: Atmospheres* 125, e2019JD031833.

Levitus, S., (1982). *Climatological Atlas of the World Ocean.* NOAA Professional Paper 13, U.S. Government Printing Office, Washington D. C., 173 pp.

Ma, X., Chang, P., Saravanan, R., Montuoro, R.., Hsieh, J.-S., Wu, D., Lin, X, Wu, L., and Jing, Z. (2015). Distance influence of Kuroshio Eddies on North Pacific Weather Patterns. *Scientific Report* 5, 17785.

Ma, X., Chang, P., Saravanan, R., Montuoro, R.., Nakamura, D., Wu, D., Lin, X, Wu, L., and Jing, Z. (2017). Importance of resolving Kuroshio front and eddy influence in simulating North Pacific storm tracks *J. Climate* 30, 1861–1880.

Mariotti, A., Baggett, C., Barnes, E. A., Becker, E., Butler, A., Collins, D. C., Dirmeyer, P. A., Ferranti, L., Johnson, N. C., Jones, J., Kirtman, B. P., Lang,

A., Molod, A., Newman, M., Robertson, A. W., Schubert, S., Waliser, D. E., and Albers, J. (2020). Windows of opportunity for skillful forecasts subseasonal to seasonal and beyond *Bull. Amer. Meteor. Soc.* 101, E608–E625.

Mak, M., (1994). Cyclogenesis in a conditionally unstable moist baroclinic atmosphere. *Tellus* 46A, 14–33.

Mosedale, T. J., Stephenson, D. B., Collins, M., and Mills, T. C., (2006). Granger causality of coupled climate process: Ocean feedback on the North Atlantic Oscillation. *J. Climate* 19, 1182–1194.

Nakamura, H., Sampe, T., Tanimoto, Y., and Shimpo, A. (2004). Observed associations among storm tracks, jet streams and midlatitude oceanic fronts. *in Earth's Climate: The Ocean-Atmosphere Interaction, Eds. C. Wang, S. P. Xie, J. A. Carton*, American Geophysical Union, 329–345.

Nakamura, H., Sampe, T., Goto, W., and Xie,, S.-P.. (2008). On the importance of midlatitude oceanic frontal zones for the mean state and dominant variability in the tropospheric circulation. *Geophys. Res. Lett.,* 35, L15709.

Orlanski, I., and Katzfey, J., (1991). Stages in the energetics of baroclinic systems. *Tellus* 47, 605–628.

Orlanski, I., Katzfey, J., and J. P. Sheldon (1995). The life cycle of a cyclone wave in the Southern Hemisphere. Part I: Eddy energy budget. *J. Atmos. Sci.,* 48, 1972–1998.

Roberston, A. W., Vitart, F., eds. (2018). *Sub-Seasonal to Seasonal Prediction: The Gap Between Weather and Climate Forecasting* Elsevier, 585 pp.

Saravanan, R., Chang, P. (2018). Midlatitude mesoscale ocean-atmosphere interaction and its relevance to S2S prediction. In *The Gap Between Weather and Climate Forecasting: Subseasonal to Seasonal Prediction,* ed. A. Roberston and F. Vitart, Elsevier, 183–200.

Small, R. J., Msadek, R., Kwon, Y.-O., Booth, J. F., Zarzycki, C. (2019). Atmosphere surface storm track response to resolved ocean mesoscale in two sets of global climate model experiments. *Climate Dynamics*, 52, 2067–2089.

Small, R. J., deSzoeke, S. P., Xie, S. P., O'Neill, L., Seo, H., Song, Q., Cornillon, P., Spall, M., Minobe S. (2008). Air-sea interaction over ocean fronts and eddies. *Dynamics of Atmospheres and Oceans*, 45, 274–319.

Snyder, C., Lindzen, R. S. (2008). Quasi-geostrophic wave-CISK in an unbounded baroclinic shear. *J. Atmos. Sci.*, 48, 76–86.

White, C. J., and co-authors., (2017). Potential applications of subseasonal-to-seasonal (S2S) predictions. *Met. Apps.* 24, 315–325.

Willison, J., Robinson, W. A., and Lackman, G. M. (2013). The importance of resolving mesoscale latent heating in the North Atlantic storm track. *J. Atmos. Sci.*, 70, 2234–2249.

Woollings, T., Hoskins, B., Blacjburn, M., Hassell, D., and Hodges, K. (2010). Storm track sensitivity to sea surface temperature resolution in a regional atmosphere model. *Clim. Dyn.*, 35, 341–353.

Wilks, D. S., (1982). *Statistical Methods in the Atmospheric Sciences.* 2nd ed. Academic Press, 627 pp.

Xie, S. P., (2004). Satellite observations of cool ocean-atmosphere interaction. *Bull. Amer. Meteorol. Soc.*, 85, 274–319.

Zhang, C., Liu, H., Xie J., Lin P., Li, C., Yang, Q., Song, J., (2020). North Pacific storm track response to the mesoscale SST in a global high-resolution atmospheric model. *Climate Dynamics*, 55, 1597–1611.

Zuidema, P., (2016). Challenges and prospects for reducing coupled climate model SST biases in the eastern tropical Atlantic and Pacific Oceans: The U.S. CLIVAR Eastern Tropical oceans Synthesis Working Group. *Bull. Amer. Meteorol. Soc.*, 97, 2305–2327.